Journal of
Materials Chemistry C

ROYAL SOCIETY
OF CHEMISTRY

PAPER

View Article Online
View Journal | View Issue

Check for updates

Cite this: *J. Mater. Chem. C*, 2024, **12**, 13411

Received 8th May 2024,
Accepted 14th July 2024

DOI: 10.1039/d4tc01873g

rsc.li/materials-c

f → f transition luminescence of Eu^{2+} in barium–aluminum–borate oxyfluoride glass ceramics

Mingjun Zhao,[ab] Panting Wang,[ab] Chongyun Shao,[a] Weichang Li,[a]
Danping Chen *[a] and Wei Chen *[a]

Novel transparent luminescent glass ceramics with the ability to generate the line emission of Eu^{2+} ions were successfully prepared. First, Eu^{2+}-doped barium–aluminum–borate oxyfluoride glasses were prepared by high-temperature melting in a reducing atmosphere, and then transparent glass ceramics were obtained by crystallization heat treatment. Fluorescence spectroscopy showed that Eu^{2+} exhibited only broadband luminescence (FWHM ≈ 136 nm) of the $4f^65d^1 \rightarrow 4f^7$ transition in the glasses. However, after heat treatment, a 359 nm line emission (FWHM ≈ 2.8 nm) from the $4f^7 \rightarrow 4f^7$ transition of Eu^{2+} appeared in the glass ceramics. To explore the mechanism of transformation of the optical transition of Eu^{2+} from $4f^65d^1 \rightarrow 4f^7$ to $4f^7 \rightarrow 4f^7$, the glasses and glass ceramics were analyzed by fluorescence spectroscopy, X-ray diffraction (XRD), Raman spectroscopy, and electron paramagnetic resonance (EPR) spectroscopy measurements. The results showed that the alteration in the optical transition of Eu^{2+} was a result of the Eu^{2+} ions entering the Ba^{2+} sites with weak crystal field strength in $BaAlBO_3F_2$ (BABF) crystals from the strong crystal field strength glass phase.

1. Introduction

Rare earth ions are indispensable activating ions in laser materials due to their abundance of energy levels.[1,2] Based on the transition selection rules, it is easier for the f → f transition to achieve laser output due to their superior optical stability, narrowband emission (high emission cross-section), and long fluorescence lifetime.[3] At present, the rare earth ions that can generate laser output and have practical applications are basically the trivalent rare earth ions of the 4f → 4f electronic transition, such as Nd^{3+}, Yb^{3+}, Er^{3+}, Ho^{3+}, and Tm^{3+}. The output wavelengths of the lasers produced by these ions are primarily located in the infrared spectral region.

A few rare earth ions can generate d → f transitions between different configurations, such as Ce^{3+} and Eu^{2+} ions. Compared with the f → f transition, the d → f transition presents challenges in achieving laser output due to its optical instability, broadband emission (low emission cross-section), and short fluorescence lifetime. Despite Eu^{2+} ions exhibiting excellent luminescence efficiency in various matrix materials and having numerous uses in the field of lighting, there are no reports on the successful laser output of Eu^{2+} ions. Some researchers have found that Eu^{2+} ions have strong $4f^65d$ excited-state absorption (ESA), which is the main reason why the 5d → 4f transition cannot achieve laser output.[4]

At present, only a small percentage of lasers directly emit visible light, and the majority of lasers emit in the infrared region. With the development of semiconductor lasers towards shorter wavelengths, the possibility of using short-wavelength LD or LED excitation of rare-earth ions to create visible lasers for applications may be achievable. To realize this dream, the first step is to look for short-wavelength f → f transition rare-earth ions. Recently, we discovered a new luminescence at approximately 359 nm after microcrystallization of glass when we were investigating the luminescence of Eu^{2+} in barium–aluminum–borate oxyfluoride glass. Out of curiosity, we investigated the origin of this new luminescence. Some studies consider that it originates from the 4f → 4f transition of Eu^{2+} and only occurs in a few fluoride crystals with weak crystal field environments.[5–8] Therefore, it can be inferred that a relatively uncommon crystal with weak field strength has formed in the glass ceramics of the oxyfluoride glass. Due to the potential application in lasers, the 4f → 4f transition of Eu^{2+} ions has received attention and been investigated.[9–11] However, at present, achieving a laser output of Eu^{2+} is still a huge challenge in the field of laser materials.

Glass ceramics doped with rare earth ions have high quantum efficiency and favorable chemical and physical properties. Meanwhile, their low cost, short preparation period, and simple preparation process make them an attractive material for optical applications. To the best of our knowledge, the 4f → 4f

---

[a] *Key Laboratory of Materials for High Power Laser, Shanghai Institute of Optics and Fine Mechanics, Chinese Academy of Sciences, Shanghai 201800, PR China. E-mail: d-chen@mail.siom.ac.cn, weichen@siom.ac.cn*

[b] *Center of Materials Science and Optoelectronics Engineering, University of Chinese Academy of Sciences, Beijing 100049, PR China*

transition of Eu^{2+} has not been reported in glass ceramics. Therefore, the development of a new type of transparent glass-ceramic material that can produce Eu^{2+} line emission has great significance in the fields of ultraviolet solid lasers, phototherapy lamps, and spectral correction. Due to the shielding effect of the outer electrons on the 4f energy level, the f → f transition emission peak is generally located near 359 nm and is hardly influenced by the matrix material.[5,12,13] The 359 nm line emission in the UVA (320–380 nm) region endows Eu^{2+} ions with potential for application in the field of UVA phototherapy lamps. UVA phototherapy lamps combined with psoralen as a photosensitizer (PUVA) lead to a phototoxic response, which is essential for the treatment of fibrotic skin diseases such as scleroderma and urticaria pigmentosa.[14,15]

In this study, a new transparent glass-ceramic material with the ability to generate the 4f → 4f transition of Eu^{2+} ions was proposed and prepared. The effects of Eu_2O_3 concentration and heat treatment conditions on the spectral properties of Eu^{2+} were studied. Fluorescence spectroscopy, XRD, Raman spectroscopy, and EPR spectroscopy measurements were used to analyze and explain the mechanism of different optical transition types of Eu^{2+} ions in the glass and glass-ceramic samples.

2. Experimental

2.1 Sample preparation

$5BaO–35BaF_2–40B_2O_3–20Al_2O_3–xEu_2O_3$ (x = 0.05–0.2) (mol%) glass samples were prepared *via* high-temperature melting. The raw materials used in the experiments were $BaCO_3$ (Aladdin, 99.8%), BaF_2 (Macklin, 99.99%), H_3BO_3 (Aladdin, AR), $Al(OH)_3$ (Aladdin, 99.9%), and Eu_2O_3 (Aladdin, 99.99%). The amount of raw materials was calculated and weighed based on the glass composition. After mixing evenly, 40 g of the mixture was transferred to a graphite crucible while keeping the Al_2O_3 crucible outside the graphite crucible to prevent excessive combustion of the graphite crucible. The graphite crucible was used to reduce Eu^{3+} to Eu^{2+} during melting. The mixture was placed in a box-type resistance furnace, heated from room temperature to 1300 °C, and maintained at that temperature for 10 min. After the mixture was completely melted, the melt was quickly poured into an Al mold and then placed in a 470 °C annealing furnace for 3 h to eliminate the stress. After cutting and polishing, the required glass samples were obtained. The glass samples were labeled E_x, where E represents Eu_2O_3, and x is 100 times the Eu_2O_3 doping content (mol%) in the sample. Then, the glass-ceramic samples were prepared by heat treatment near the glass crystallization temperature. The glass samples were placed in a double-layer Al_2O_3 crucible containing charcoal powder, which was used to create a CO atmosphere that prevented the oxygen-induced uneven crystallization of the glass samples. The double-layer Al_2O_3 crucible was heated in a box-type resistance furnace at 570 or 580 °C for 2 or 2.5 h and allowed to cool naturally to room temperature before removal. The obtained glass-ceramic samples were labeled E_xT-y h, where T is the heat treatment temperature, y is the heat treatment time, and h is the abbreviation for hours. For example, E_{15}570-2h represents the glass-ceramic sample obtained by heat treatment of a 0.15 mol% Eu_2O_3-doped glass sample at 570 °C for 2 h.

2.2 Characterization

Differential scanning calorimetry (DSC) curves of the glass samples were obtained using a Netzsch 404 differential scanning calorimeter. Density was measured using a Japan Alfa Mirage D-200L electronic densitometer. The refractive index of the glass was measured using a prism coupler (Model 2010/M, Mectricon, USA) with a 633 nm laser. The crystallization status after crystallization heat treatment was assessed using a Smartlab9 X-ray diffractometer (Rigaku, Japan), with a Cu-Kα line as the X-ray source. Transmission spectra were obtained using a PerkinElmer Lambda 950 UV/VIS/NIR spectrophotometer with a test range of 300–650 nm and a test step of 1 nm. The excitation and emission spectra, as well as the fluorescence decay lifetime of the samples, were measured using an FLS 1000 fluorescence spectrometer (Edinburgh Instruments). The continuous-wave (CW) EPR spectra (X-band, ~9.37 GHz) of the samples were measured at room temperature using an E-580 electron paramagnetic resonance spectrometer (Bruker, Germany). The Raman spectra were measured using a Renishaw InVia micro-Raman spectrometer with a laser wavelength of 785 nm and in a testing range of 100–1500 cm^{-1}. All the above tests were performed at room temperature.

3. Results and discussion

3.1 Characterization of the crystallization status

To investigate the glass stability and crystallization temperature of the glass samples, the E_{15} glass sample doped with 0.15 mol% Eu_2O_3, which had the highest fluorescence intensity among all the glass samples shown in Fig. 4, was selected for the DSC curve test. According to the DSC curve shown in Fig. 1, the transition temperature T_g of the E_{15} glass sample is 491 °C. Beyond the transition temperature, a sharp exothermic crystallization peak appears, at an initial crystallization temperature T_x of 570 °C. The sharp crystallization peak indicates that the glasses have strong crystallization ability. Therefore, to obtain higher transparency in the glass-ceramic samples, in this study, the glass samples were heat-treated at 570 °C and 580 °C (near the initial crystallization temperature) for 2 h and 2.5 h, respectively.

To investigate the crystallization status of the samples, the E_{15}-series glass and glass-ceramic samples doped with 0.15 mol% Eu_2O_3 were selected for XRD and Raman measurements. Fig. 2(a) shows the XRD patterns of the E_{15}-series glass and glass-ceramic samples. In Fig. 2(a), the E_{15} sample exhibits an amorphous scattering peak, indicating that it is in a disordered glassy state. As the heat treatment temperature and time increase, sharp diffraction peaks gradually appear in the XRD pattern, indicating that the number and size of the microcrystals formed in the samples increase. This results in a decrease in the transparency of the samples and an increase

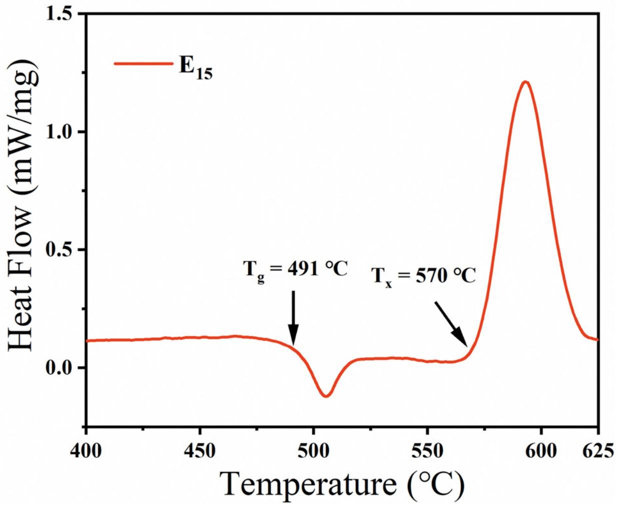

Fig. 1 DSC curve of the E_{15} glass sample.

in the intensity of the line emission peak of Eu^{2+}, which will be discussed subsequently. The bottom line in Fig. 2(a) shows the standard XRD pattern (ICSD card # 409663) of the $BaAlBO_3F_2$ (BABF) crystal. The positions of the diffraction peaks of the E_{15}580-2h and E_{15}580-2.5h samples are consistent with those of the BABF crystals, indicating that the crystals precipitated in the glass ceramics are BABF crystals.

Fig. 2(b) shows the normalized Raman spectra of the E_{15}-series glass and glass-ceramic samples. After heat treatment, new sharp Raman peaks gradually appear at 130, 275, 350, 470, and 985 cm^{-1} in the glass-ceramic samples. Shionozaki and Du *et al.*[16,17] also observed Raman vibration peaks at 350, 470, and 985 cm^{-1} in the range of 140–1400 cm^{-1} in glass ceramics containing BABF crystals, which were attributed to the bending or stretching modes of the BO_3 units in BABF crystals. Zhuravlev *et al.*[18] summarized the Raman spectra of the BABF crystal, where the Raman peak at 134.5 cm^{-1} corresponds to the E'' and E_{1g} vibrational modes and the Raman peak at 270.4 cm^{-1} corresponds to the E', E_g, E', and E_{2g} vibrational modes. Therefore, the appearance of sharp peaks in the Raman spectra also indicates that nonlinear BABF crystals precipitated in the glass-ceramic samples.

In Fig. 2, the XRD pattern of the E_{15}570-2h sample does not show any notable crystal diffraction peaks. Similarly, the Raman spectra of the E_{15}570-2h sample also does not display any apparent crystal Raman peaks. However, combined with the EPR (Fig. 7) and fluorescence (Fig. 6) test results, it can be inferred that a trace quantity of the BABF crystal forms successfully within the E_{15}570-2h sample. Due to the small size and number of microcrystals, the presence of BABF microcrystals in the E_{15}570-2h sample could not be determined using XRD or Raman spectroscopy.

Table 1 displays the densities of the E_{15}-series glass and glass-ceramic samples. The density of the nonlinear crystal BABF was reported to be 4.47 g cm^{-3}.[17,19] According to Table 1, the density of the E_{15} glass sample is 3.700 g cm^{-3}. Compared with the arranged and compact structure of the crystal, glass has a looser and more disordered structure, resulting in a lower density. With an increase in the degree of microcrystallinity, the size and number of BABF crystals that precipitated in the sample increased. This led to a denser structure and a steady increase in the density of the glass ceramics.

Fig. 3(a) displays the actual images of all glass and glass-ceramic samples. Fig. 3(b) shows the transmittance of the glass and glass-ceramic samples at 550 nm. As depicted in Fig. 3(a) and (b), the prepared glass samples all exhibit exceptional transparency, with a transmittance of 94% in the visible range of 450–550 nm. The transparency of the samples decreases to varying degrees as the heat treatment temperature and time increase, and the transmittance in the visible region gradually decreases from ∼94% to ∼11%. Combined with the XRD results, it is explained that the light scattering degree of the glass-ceramic samples gradually increases with an increase in the size and number of BABF microcrystalline particles.

The refractive index of the matrix glass E_{15} was measured to be 1.5687 (λ = 633 nm). The BABF crystal that precipitated in

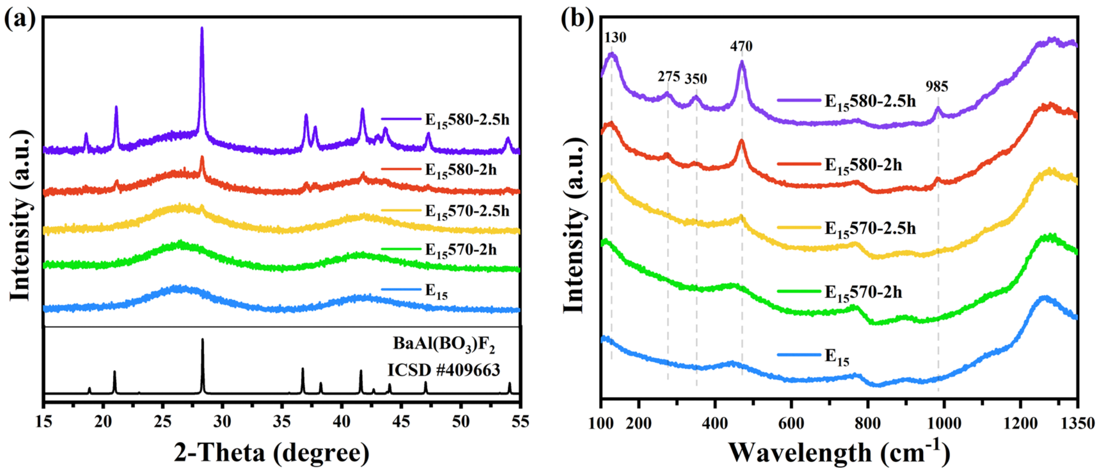

Fig. 2 (a) XRD and (b) Raman spectra of the E_{15}-series glass and glass-ceramic samples.

Table 1 Densities of the E_{15}-series glass and glass-ceramic samples

Sample	E_{15}	E_{15}570-2h	E_{15}570-2.5h	E_{15}580-2h	E_{15}580-2.5h
Density (g cm^{-3})	3.700	3.706	3.709	3.722	3.779

the glass ceramics had a hexagonal crystal structure and was a nonlinear crystal with a refractive index of n_o = 1.6284 and n_e = 1.5850 (λ = 633 nm).[20] To maintain optimal transparency in glass ceramics, it is important to minimize the refractive index difference between the precipitated crystal and the matrix glass. Furthermore, it is desirable for the crystal to possess high symmetry or for the precipitated crystal particles to be relatively small in size. This glass ceramic exhibited notable light scattering owing to the difference in the refractive index between the glass and the precipitated crystal. The precipitated crystal, which belongs to the hexagonal crystal system with lower symmetry, further contributed to this scattering effect. As a result, the transmittance of the glass ceramic was greatly reduced when the crystal grew slightly.[21]

As shown in Fig. 3(b), the transmittance of the samples remains relatively stable as the amount of Eu_2O_3 doping increases under the same heat treatment conditions. This suggests that variations in the content of Eu_2O_3, ranging from 0.05 to 0.2 mol%, have little impact on the crystallization ability of the glasses. The degree of crystallization of the glass-ceramic samples was mainly related to the heat treatment conditions.

Fig. 3(c) shows the transmission spectra of the E_x glass samples doped with varying amounts of Eu_2O_3. The figure shows that an increase in the doping amount of Eu_2O_3 from 0.05 mol% to 0.2 mol% results in a redshift of the UV absorption edge and deepening of the pale yellow color of the glass sample (Fig. 3(a)). This is due to the increased number of Eu^{2+} ions in the glass sample, which enables stronger absorption within the 250–450 nm range *via* the electric dipole transition $4f^7 \rightarrow 4f^65d^1$ of Eu^{2+}.

Fig. 3(d) shows the transmission spectra of the E_{15}-series glass and glass-ceramic samples doped with 0.15 mol% Eu_2O_3. The UV absorption edge of the E_{15} glass shown in Fig. 3(d) is approximately 376 nm, and the absorption end of the glass ceramics remains relatively constant with increasing degree of microcrystallinity. This is because the difference in composition between the precipitated crystals and the glass is very small.

3.2 Dependence of the spectral properties on the Eu_2O_3 concentration

Fig. 4 displays the excitation and emission spectra of the E_x glass samples doped with different Eu_2O_3 concentrations to investigate the impact of the Eu_2O_3 concentrations on the broadband emission of Eu^{2+}. Fig. 4(a) shows the excitation spectra obtained by monitoring the optimal emission wavelength of the E_x glass samples. Broadband excitation at 250–430 nm can be attributed to the transition of Eu^{2+} ions from the $4f^7(^8S_{7/2})$ ground state to the $4f^65d^1$ excited state. In Fig. 4(b), the broadband emission peak centered at approximately 495 nm corresponds to the $4f^65d^1 \rightarrow 4f^7(^8S_{7/2})$ transition of Eu^{2+}.[22] It is evident that the broadband emission intensity first increases as the amount of Eu_2O_3 doping increases. As the concentration increases to approximately 0.15 mol%, the E_{15} glass sample exhibits the highest emission intensity, and then the excessive Eu^{2+} concentration causes non-radiative relaxation, resulting in luminescence quenching. Furthermore, the emission peak shifts towards longer wavelengths, which is attributed to the nephelauxetic effect caused by the higher Eu^{2+} concentration. This effect decreases the $5d(t_{2g})$ energy level, which results in the transition energy between the

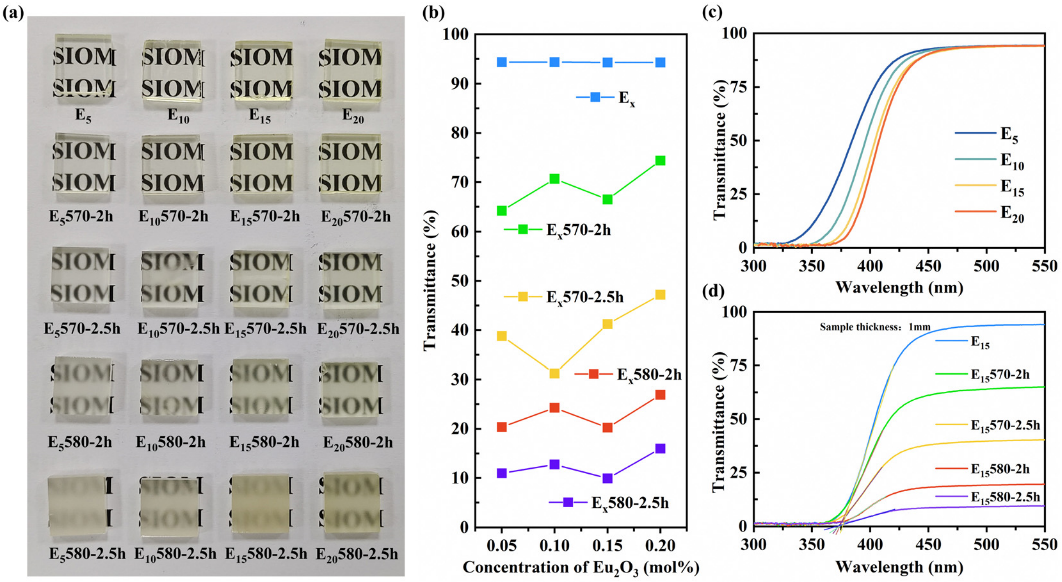

Fig. 3 (a) Actual images of all samples; (b) transmittance of samples at 550 nm; (c) transmission spectra of the E_x glass samples; and (d) transmission spectra of the E_{15}-series glass and glass-ceramic samples. The sample thickness was 1 mm.

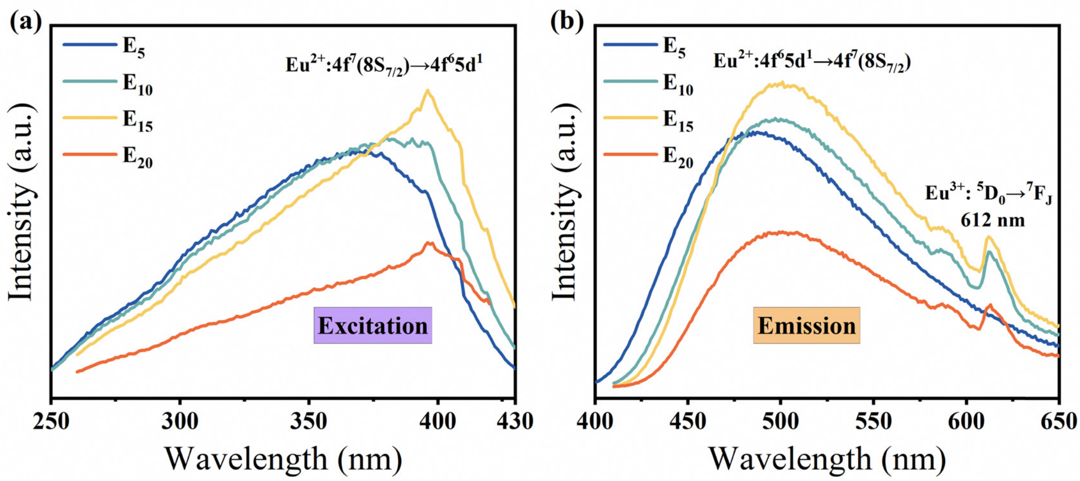

Fig. 4 (a) Excitation and (b) emission spectra of the E_x glass samples.

energy levels shifting in lower-energy directions.[22] In Fig. 4(b), the weak emission peak near 612 nm in the E_{10}, E_{15}, and E_{20} samples corresponds to the $^5D_0 \rightarrow {}^7F_2$ transition of Eu^{3+}. This is due to the limitation of the reduction capacity during the preparation process. The increase in the Eu_2O_3 doping concentration in the sample resulted in the excess Eu^{3+} ions not being reduced to Eu^{2+} ions but remaining in the glass as Eu^{3+} ions.

Fig. 5(a) shows the excitation spectra of E_x and E_x570-2h samples at a monitoring wavelength of 359 nm. Fig. 5(b) shows the emission spectra of E_x and E_x570-2h samples doped with different Eu_2O_3 concentrations under 257 nm excitation. In Fig. 5(b), the bump in the emission spectra at 370–400 nm corresponds to the $4f^65d^1 \rightarrow 4f^7(^8S_{7/2})$ transition of Eu^{2+}. Compared with the E_x glass samples, the emission spectra of the E_x570-2h samples after heat treatment show a new UV-sharp emission peak at 359 nm. The excitation spectra of the 359 nm peak are broad, spanning from 220 to 350 nm, with a maximum excitation peak located at 257 nm.[13] This line emission can be assigned to the $4f^7(^6P_{7/2}) \rightarrow 4f^7(^8S_{7/2})$ transition of Eu^{2+} ions in the weak crystal field. In addition, the $4f^7(^6P_{7/2}) \rightarrow 4f^7(^8S_{7/2})$ transition of Eu^{2+} ions can be excited by a LED because LEDs with a wavelength of 254 nm have been commercialized.

The 4f shell of Eu^{2+} is half-filled, and its ground state is $4f^7(^8S_{7/2})$, with the two lowest excited states being $4f^7(^6P_{7/2})$ and $4f^65d(t_{2g})$. Generally, $5d(t_{2g})$ is located below the $4f^7(^6P_{7/2})$ energy level at room temperature. Therefore, in most Eu^{2+}-doped materials, only 5d → 4f transitions can be observed, and forbidden 4f → 4f transitions cannot be observed.[5] Hewes and Hoffman observed the 361 nm line emission of the $4f^7(^6P_{7/2}) \rightarrow 4f^7(^8S_{7/2})$ transition of Eu^{2+} in the $BaAlF_5$ crystal.[13,23] Some studies have found that the 4f → 4f transition of Eu^{2+} only occurs in a few fluoride crystals with weak crystal field environments.[5–8]

Therefore, considering the XRD test results, the observation of the $4f^7(^6P_{7/2}) \rightarrow 4f^7(^8S_{7/2})$ transition in the glass-ceramic samples indicates that a part of the Eu^{2+} ions enters the BABF crystal phase from the glass phase, and the crystal field strength around Eu^{2+} ions in the BABF crystals is weak compared to that in the glass matrix.

In Fig. 2, the XRD and Raman test results did not show any significant structural changes between the E_{15}570-2h and E_{15} glass samples. However, in Fig. 5(b), the appearance of an obvious narrowband emission indicates that there is indeed precipitation of BABF crystals in the E_{15}570-2h sample after heat treatment at 570 °C for 2 h, which implies that the Eu^{2+}

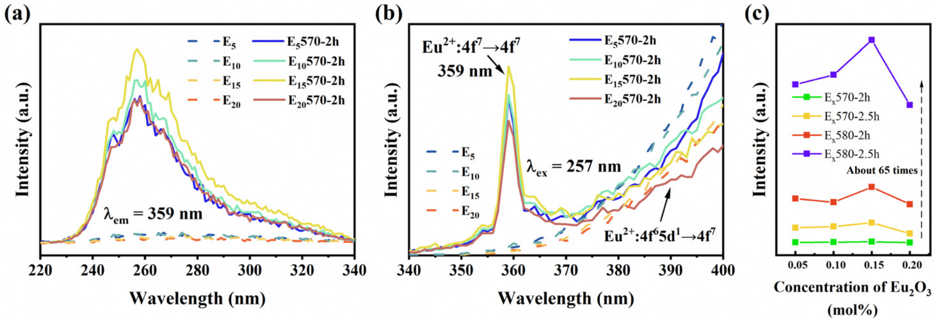

Fig. 5 (a) Excitation spectra of E_x and E_x570-2h samples monitored at 359 nm; (b) emission spectra of E_x and E_x570-2h samples under 257 nm excitation; and (c) emission peak intensities of all glass-ceramic samples at 359 nm.

fluorescence spectra are more sensitive for detecting the formation of BAB crystals. This could be a more efficient and easier way to qualitatively or quantitatively analyze the precipitation of BABF crystals in glass ceramics.

To study the dependence of the line emission spectra of Eu^{2+} on the Eu_2O_3 doping amount, Fig. 5(c) shows the 359 nm emission peak intensity of all glass-ceramic samples under 257 nm excitation. This demonstrates that the 359 nm emission peak intensity of the glass-ceramic samples does not exhibit a linear relationship with the doped Eu_2O_3 concentration under the same heat treatment conditions. There occurs a fluorescence quenching after the doped Eu_2O_3 concentration exceeds 0.15 mol%. Meanwhile, the 359 nm emission peak intensity of the glass-ceramic samples significantly increases as the heat treatment temperature and time increase. Obviously, the intensity of the 359 nm emission peak mainly depends on the degree of microcrystallization due to heat treatment. We selected the E_{15} series of glass and glass-ceramic samples with high fluorescence peak intensities for XRD, fluorescence spectroscopy, EPR spectroscopy, and Raman spectroscopy measurements to investigate the effect of the heat treatment conditions on the spectral properties of the samples.

3.3 Dependence of the spectral properties on the heat treatment conditions

Fig. 6(a) shows the excitation spectra with broadband emission peaks for the E_{15}-series glass and glass-ceramic samples. The excitation peak is broad in the range of 260–480 nm with a maximum excitation peak located at 398 nm, which corresponds to the $4f^7(^8S_{7/2}) \rightarrow 4f^65d^1$ transitions of Eu^{2+}. Fig. 6(b) shows the broadband emission spectra of the $4f^65d^1 \rightarrow 4f^7(^8S_{7/2})$ transition of Eu^{2+} with an optimal excitation peak at 398 nm, which has a full width at half-maximum (FWHM) of approximately 136 nm. As the degree of microcrystallinity increases, the broadband emission intensity first increases and then weakens, and the emission wavelength of the E_{15}580-2.5h sample blue-shifts to 490 nm. This suggests that the d → f transition is also influenced by the degree of microcrystallization, which will be discussed in detail in Section 3.4.

Fig. 6(d) shows that the excitation spectra of the line emission are broad in the range of 240–330 nm with a maximum excitation peak located at 257 nm. Fig. 6(e) shows the emission spectra of the glass and glass-ceramic samples with an optimal excitation peak at 257 nm. The legend of Fig. 6(e) is the same as that of Fig. 6(d). The emission spectra of the glass-ceramic samples simultaneously show a broadband emission peak corresponding to the $4f^65d^1 \rightarrow 4f^7$ transition and a 359 nm line emission peak associated with the $4f^7 \rightarrow 4f^7$ transition.[23] The FWHM of the line emission peak is approximately 2.8 nm, which is consistent with the characteristics of the $4f^7 \rightarrow 4f^7$ optical transition. To make it clear that the 359 nm luminescence peak was caused by Eu^{2+}, a control sample of the $E_0$580-2.5h glass ceramic without Eu_2O_3 doping was prepared. As shown in Fig. 6(e), the $E_0$580-2.5h glass-ceramic sample does not exhibit a 359 nm emission peak. This further indicates that this emission peak is not derived from the crystals precipitated from the glass-ceramic sample but from Eu^{2+} in the BABF crystal phase.

The inset (i) in Fig. 6(e) shows the emission spectra of the E_{15}570-2h sample under 257 nm excitation. The fluorescence of E_{15}570-2h is dominated by broadband emission, and the line emission intensity is relatively low. However, the intensity of the 359 nm line emission peak of Eu^{2+} gradually increases as the microcrystalline degree increases. The 359 nm peak intensity of the E_{15}580-2.5h sample is approximately 65 times higher than that of the E_{15}570-2h sample. Fig. 6(e) shows that the

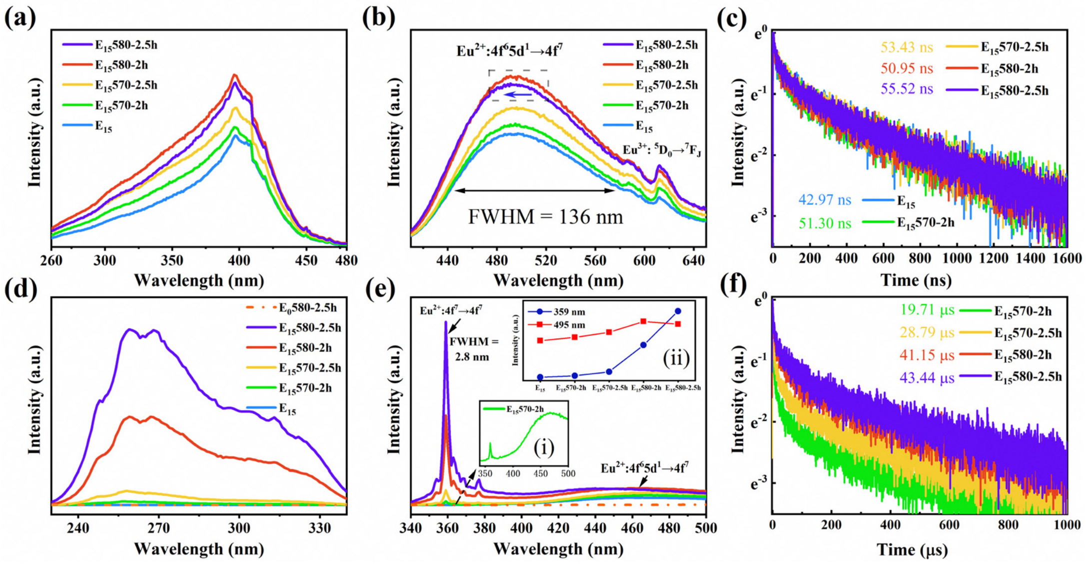

Fig. 6 (a) Excitation spectra, (b) emission spectra, and (c) fluorescence decay lifetime of the d → f transition. (d) Excitation spectra, (e) emission spectra, and (f) fluorescence decay lifetime of the f → f transition. Inset (i) shows the emission spectra of the E_{15}570-2h sample. Inset (ii) shows the intensities of the emission peaks at 359 nm and 495 nm.

fluorescence of the E_{15}580-2.5h sample occurs mainly in the 359 nm line emission, and the broadband emission is weak and can be ignored.

The inset (ii) in Fig. 6(e) shows the intensity of two different emission peaks for the E_{15}-series glass and glass-ceramic samples excited at their respective optimal excitation wavelengths. The optimal excitation wavelengths for 359 nm and 495 nm are 257 nm and 398 nm, respectively. The inset (ii) demonstrates that the intensity of the line emission peak at 359 nm exceeds that of the broadband emission peak at 495 nm for the E_{15}580-2.5h sample. These findings indicate that the E_{15}580-2.5h glass-ceramic sample exhibits superior narrowband luminescence properties.

As shown in Fig. 6(a) and (e), there is an overlap between the 359 nm emission of the f → f transition and the excitation spectra of the d → f transition, indicating that reabsorption and energy transfer may occur between the f → f and d → f transitions. However, the excitation spectra in Fig. 6(a) do not show the energy transfer from the f → f transition to the d → f transition. This phenomenon can be attributed to the fact that the d → f transition Eu^{2+} ions are mainly present in the glass matrix, whereas the f → f transition Eu^{2+} ions are only found in the crystal matrix. The significant distance between the Eu^{2+} ions located in distinct matrix environments limits the transfer of energy. Section 3.4 suggests the existence of the f → f and d → f transitions of Eu^{2+} in the BABF crystal. The Eu^{2+} ions within the crystal are relatively close together, and there is a possibility of energy transfer. However, the limited quantity of the d → f transition Eu^{2+} ions present in the crystal results in a rather feeble impact of energy transfer on the fluorescence of both the f → f and d → f transitions.

Fig. 6(f) shows that the fluorescence lifetime increases from approximately 19 μs to 43 μs as the degree of microcrystallinity increases. This indicates that a reabsorption process should occur between the f → f and d → f transitions. Due to the low f → f transition emission intensity of the E_{15}570-2h sample, it is susceptible to the reabsorption process, resulting in a shorter fluorescence lifetime. However, the reabsorption is weak, and the emission of the f → f transition remains largely unaffected by reabsorption. The 359 nm emission peak can still be observed in the fluorescence spectrum.

Fig. 6(c) and (f) show the fluorescence decay lifetime of the broadband emission and the line emission of the samples, respectively. The broadband emission has a lifetime of approximately 50 ns, whereas the fluorescence lifetime of the 359 nm line emission is much longer, approximately 30 μs. This is consistent with the characteristics of the $4f^65d^1 \rightarrow 4f^7$ and $4f^7 \rightarrow 4f^7$ transitions.

3.4 Mechanism of alteration of the Eu^{2+} transition

Electron paramagnetic resonance (EPR) method is based on the resonance absorption of external magnetic fields by unpaired electrons and is an essential method for identifying transition metals and rare-earth ions in glass materials and analyzing their surrounding environment.[24] The electron configuration of Eu^{3+} is $4f^65s^25p^6$, and all electrons in the orbital are paired, resulting in the absence of an EPR signal. However, the electron configuration of Eu^{2+} is $4f^7$, with the 4f orbital having a half-filled structure. The presence of unpaired electrons in this orbital causes it to exhibit paramagnetic properties, and its EPR signal can be detected at room temperature.[25] EPR has emerged as a promising technique for investigating alterations in the valence states of Eu ions and the surrounding coordination environment of Eu^{2+}.[26]

Fig. 7 shows the X-band EPR spectra of the E_{15}-series glass and glass-ceramic samples at room temperature. Eu^{2+} is classified as a rare-earth S-state ion with an electronic configuration of $4f^7$, a total atomic orbital quantum number of $L = 0$, and a

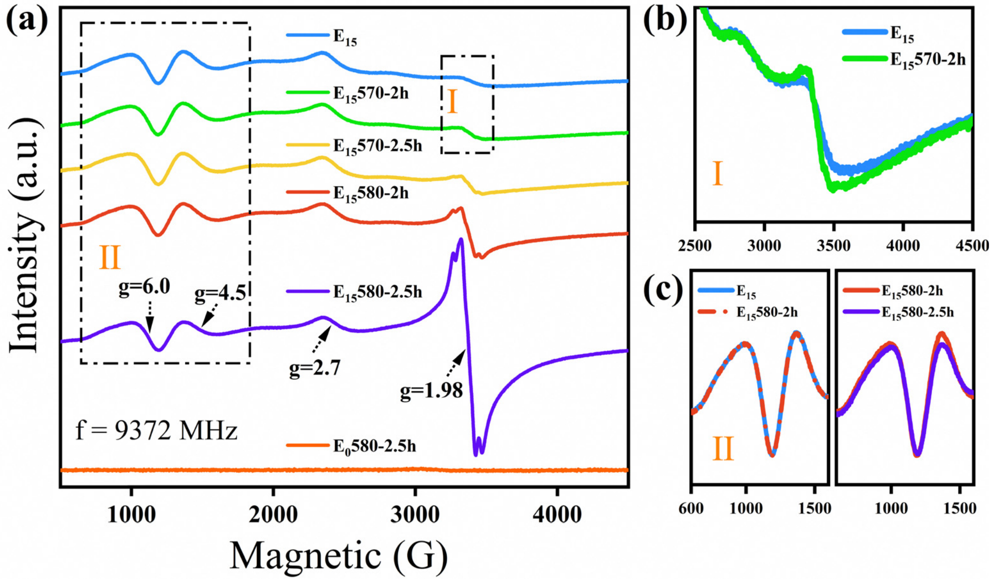

Fig. 7 (a) EPR spectra of the E_{15}-series glass and glass-ceramic samples; (b) magnified view of region I in (a); and (c) magnified view of region II in (a).

ground state of $^8S_{7/2}$. Perturbation theory studies have demonstrated that the spin Hamiltonian of S-state ions contains Zeeman and crystal field (CF) interactions. Thus, the EPR spectra depend on the relative magnitude between the Zeeman microwave frequency of the magnetic field and the strength of the crystal field:[27–29]

$$H = H_{\mathrm{Zeeman}} + H_{\mathrm{CF}} \quad (1)$$

Formula (1) consists of two terms: H_{Zeeman} is the electron Zeeman interaction, and H_{CF} is the crystal field interaction. In this study, the Zeeman microwave frequency (ν) was 9.372 GHz. When the crystal field strength significantly exceeds the Zeeman microwave frequency ($H_{\mathrm{CF}} \gg h\nu$), the EPR signal of Eu^{2+} appears at $g > 2$. When the microwave frequency is equal to the strength of the crystal field, a zero-field resonance signal can be detected. When the crystal field strength is significantly weaker than the microwave frequency ($H_{\mathrm{CF}} \ll h\nu$), the EPR signal peak can be observed near $g \approx 2.0$.[27,28]

In Fig. 7(a), the X-band EPR first-derivative spectra of Eu^{2+} in the E_{15} glass sample are dominated by wide resonance lines at $g = 6.0$, 4.5, and 2.7 characteristic signal peaks, indicating that the crystal field interaction is stronger than the Zeeman interaction. This spectrum is so ubiquitous in glassy and disordered polycrystalline materials that it is referred to as the "U" spectrum.[24,30]

As shown in Fig. 7(a) and (b), after heat treatment, a new sharp EPR signal peak appears near $g = 1.98$ in the E_{15}570-2h glass-ceramic sample, and this peak intensity gradually increases with increasing heat treatment temperature and time. Lu *et al.*[31,32] found that when Eu^{2+} occupied the Ba site of $BaTiO_3$, an EPR signal at an X-band microwave frequency of 9.148 GHz appeared at $g = 1.98$. The $E_0$580-2.5h glass-ceramic sample without Eu_2O_3 doping does not exhibit any EPR signal peak, indicating that the EPR signal peak near $g = 1.98$ is not derived from the crystals precipitated from the glass-ceramic sample but rather from Eu^{2+} in the BABF crystal phase. Therefore, the EPR test results show that after microcrystallization, a trace quantity of Eu^{2+} ions enter the BABF crystal, and the crystal field strength of some Eu^{2+} ions in the BABF is significantly weaker than the microwave frequency ($H_{\mathrm{CF}} \ll h\nu$). With an increase in microcrystallization, the number of Eu^{2+} ions entering the BABF crystal phase increases. This is the reason for the emergence and increase in the line emission peak of Eu^{2+} in the glass-ceramic samples.

As depicted in Fig. 7(c), the EPR "U" spectra of the E_{15} and E_{15}580-2h samples exhibit a high degree of overlap, indicating that the majority of the Eu^{2+} ions still remain in the glass after microcrystallization. In Fig. 7(d), the relative intensity ratio ($I_{g=4.5}/I_{g=6.0}$) between the strong and weak crystal fields of the E_{15}580-2.5h sample is slightly lower than that of the E_{15}580-2h sample. Previous studies have demonstrated that the EPR signal peak intensity ratio ($I_{g=4.5}/I_{g=6.0}$) of the "U" spectrum corelates with the coordination field strength of Eu^{2+} in the glass material. The signal peaks in the characteristic "U" spectrum of Eu^{2+} are assigned to two Eu^{2+} sites: the signal peak at $g = 6.0$ corresponds to the weak crystal field site, and the peak at $g = 4.6$ corresponds to the strong crystal field site.[25,33,34] The decrease of the intensity ratio ($I_{g=4.5}/I_{g=6.0}$) in Fig. 7(d) indicates a weakening of the crystal field strength surrounding Eu^{2+}. Therefore, the crystal field splitting of the 5d energy level of Eu^{2+} decreased, causing blueshifts of the 5d → 4f transition broadband emission peak wavelength of the E_{15}580-2.5h sample, as shown in Fig. 6(b).

Combined with the fluorescence and EPR spectra, the luminescence transition diagram of Eu^{2+} in the BABF crystal and glass phases is shown in Fig. 8. $\varepsilon_{\mathrm{cfs}}$ represents the crystal field splitting energy difference between the lowest and highest energies of the 5d state. The 4f energy level of Eu^{2+} is shielded by the external 5s and 5p orbitals, and its energy-level position is unaffected by the external environment. However, the external 5d energy level is susceptible to the influence of the external environment, resulting in its splitting into t_{2g} and e_g.[22,35] The crystal field strength and nephelauxetic effect of the surrounding environment affect the position of the 5d(t_{2g}) energy level, thereby influencing the optical transition type of Eu^{2+}.

Kunghatkar *et al.*[13] observed both broadband and narrowband emission peaks for the $BaAlBO_3F_2$:Eu^{2+} phosphor and proposed that Eu^{2+} would replace the octahedral Al^{3+} and tetrahedral Ba^{2+} sites in the BABF crystal. Broadband emission is generated if Eu^{2+} occupies the octahedral Al^{3+} site, while narrowband emission is generated when Eu^{2+} occupies the tetrahedral Ba^{2+} site.

As shown in Fig. 8(b), the crystal field strength is strong in the glass phase, and the splitting of the 5d energy level of Eu^{2+} is larger. The 5d(t_{2g}) energy level is lower than that of $4f^7(^6P_{7/2})$,

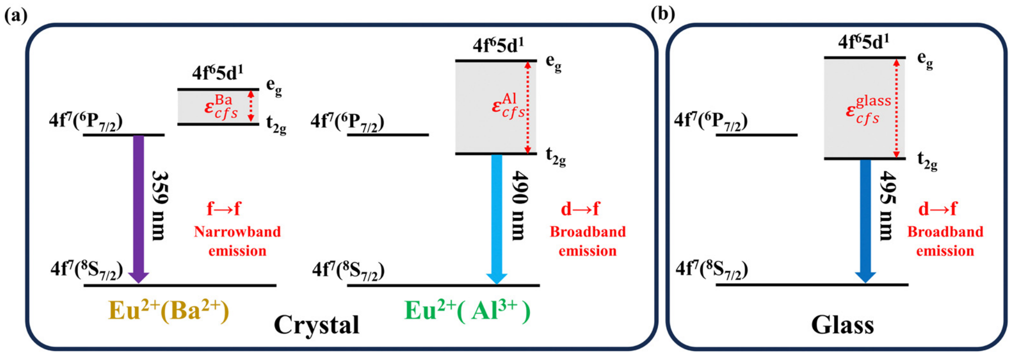

Fig. 8 Schematic of the luminescence transition of Eu^{2+} in the (a) BABF crystal phase and (b) glass phase.

resulting in a characteristic broadband emission peak of the 5d → 4f transition.

After crystallization, some of the Eu^{2+} ions in the glass phase enter the Ba^{2+} sites in the BABF crystal phase. As shown in Fig. 8(a), the extremely weak crystal field strength surrounding the Ba^{2+} site $\left(\varepsilon_{\mathrm{cfs}}^{\mathrm{Ba}^{2+}} \ll \varepsilon_{\mathrm{cfs}}^{\mathrm{glass}}\right)$ results in a small crystal field splitting of Eu^{2+}, and the $5d(t_{2g})$ energy level is higher than the $4f^7(^6P_{7/2})$ energy level. Therefore, the Eu^{2+} ion optical transition transforms from the $4f^65d^1 \rightarrow 4f^7$ transition to the $4f^7 \rightarrow 4f^7$ transition, resulting in a line luminescence peak in the glass-ceramic samples.[6,13] Meanwhile, the crystal field strength around Eu^{2+} at the Ba^{2+} site is significantly weaker compared to the Zeeman microwave frequency $\left(H_{\mathrm{CF}}^{\mathrm{Ba}^{2+}} \ll h\nu\right)$, resulting in the EPR signal peak of Eu^{2+} appearing at approximately $g = 1.98$. The increase in the intensity of the 359 nm narrowband emission peak of Eu^{2+} can be attributed to an increase in the quantity of crystallites, resulting in a steady increase in the quantity of Eu^{2+} occupying the Ba^{2+} site.

As shown in Fig. 8, a portion of Eu^{2+} can occupy the Al^{3+} site in the BABF crystal. Compared with that in the glass matrix, the crystal field strength surrounding the Eu^{2+} ions at the Al^{3+} site is reduced, resulting in a weakening of the crystal field splitting $\left(\varepsilon_{\mathrm{cfs}}^{\mathrm{Ba}^{2+}} \ll \varepsilon_{\mathrm{cfs}}^{\mathrm{Al}^{3+}} < \varepsilon_{\mathrm{cfs}}^{\mathrm{glass}}\right)$. However, the $5d(t_{2g})$ energy level is still lower than the $4f^7(^6P_{7/2})$ energy level. Therefore, the optical transition of Eu^{2+} at the Al^{3+} site is still the $4f^65d^1 \rightarrow 4f^7$ transition, but the wavelength of broadband emission is shorter than that in the glass phase.[13] Moreover, the crystal field strength around Eu^{2+} at the Al^{3+} site is still stronger than the Zeeman microwave frequency $\left(h\nu \ll H_{\mathrm{CF}}^{\mathrm{Al}^{2+}} < H_{\mathrm{CF}}^{\mathrm{glass}}\right)$. Eu^{2+} still exhibits a characteristic ''U'' spectrum, but its relative intensity ratio $(I_{g=4.5}/I_{g=6.0})$ decreases due to the weakening of the crystal field.

Meanwhile, when Eu^{2+} enters the Al^{3+} site after microcrystallization, a decrease in phonon energy and a reduction in non-radiative relaxation in the crystals lead to an enhanced broadband emission intensity, as shown in Fig. 6. However, if the degree of microcrystallization continues to increase, a large proportion of Eu^{2+} will occupy the Ba^{2+} site because Eu^{2+} ions approach Ba^{2+} in terms of the valence state and ionic radius. A reduction in the quantity of Eu^{2+} that generates the d → f transition results in a decrease in the broadband emission intensity.

4. Conclusions

In summary, the f → f transition line emission of Eu^{2+} ions in transparent luminescent glass ceramics was successfully observed. Eu^{2+}-doped oxyfluoride borate glasses were prepared under reduction conditions, and transparent glass ceramics containing BABF microcrystalline particles were successfully prepared by heat treatment under a CO atmosphere. A broadband emission peak (FWHM ≈ 136 nm) was observed at around 495 nm for the glass sample, which was caused by the $4f^65d^1 \rightarrow 4f^7(^8S_{7/2})$ transition of Eu^{2+}. However, the glass ceramics obtained after heat treatment not only exhibited this broadband luminescence peak but also exhibited a new line luminescence peak (FWHM ≈ 2.8 nm) at 359 nm. The structural and optical properties of the glass and glass-ceramic samples were analyzed using XRD, Raman spectroscopy, fluorescence spectroscopy, and EPR spectroscopy measurements. The results showed that the new line emission was derived from the $4f^7(^6P_{7/2}) \rightarrow 4f^7(^8S_{7/2})$ transition of Eu^{2+} at the Ba^{2+} sites in the BABF crystal. The Eu^{2+} transition type was determined by the surrounding crystal field strength. After crystallization, some Eu^{2+} ions enter the BABF crystal from the glass matrix, resulting in a decrease in the surrounding crystal field strength. Therefore, the optical transition of Eu^{2+} transforms from the $4f^65d^1 \rightarrow 4f^7(^8S_{7/2})$ transition to the $4f^7(^6P_{7/2}) \rightarrow 4f^7(^8S_{7/2})$ transition. As the degree of crystallization increased, the intensity of the 359 nm emission peak of Eu^{2+} also increased. This Eu^{2+}-doped barium–aluminum–borate oxyfluoride transparent glass ceramic material has the characteristics of a long fluorescence lifetime and narrowband emission. It is a promising material in the fields of UV solid laser materials, spectral correction, and phototherapy lamps.

Data availability

The data that support the findings of this study are available from the corresponding author (Danping Chen) upon reasonable request.

Conflicts of interest

There are no conflicts of interest to declare.

Acknowledgements

This study was supported by the National Natural Science Foundation of China (Grant No. 51872308).

References

1 B. Jiang, S. Zhu, L. H. Ren, L. Shi and X. L. Zhang, *Adv. Photonics*, 2022, **4**, 8.
2 L. P. Yu, J. H. Liang, Q. H. Zeng, J. C. Wang, X. Luo, J. Z. Wang, P. G. Yan, F. L. Dong, X. Liu, Q. T. Lue, C. Y. Guo and S. C. Ruan, *High Power Laser Sci. Eng.*, 2023, **11**, 6.
3 L. Li, J. Chen, X. Peng, T. Jiang, L. Lei and H. Guo, *J. Mater. Chem. C*, 2023, **11**, 11664–11670.
4 J. K. Lawson and S. A. Payne, *Phys. Rev. B: Condens. Matter Mater. Phys.*, 1993, **47**, 14003–14010.
5 L. Qin, P. Cai, C. Chen, J. Wang, S. I. Kim, Y. L. Huang and H. J. Seo, *J. Alloys Compd.*, 2018, **738**, 372–378.
6 R. Alcala, D. K. Sardar and W. A. Sibley, *J. Lumin.*, 1982, **27**, 273–284.
7 R. Francini, U. M. Grassano, S. Boiko, G. G. Tarasov and A. Scacco, *J. Chem. Phys.*, 1999, **110**, 457–464.

8 R. N. Hua, B. F. Lei, D. M. Xie and C. S. Shi, *J. Solid State Chem.*, 2003, **175**, 284–288.

9 H. Q. Su, Z. H. Jia, C. S. Shi, J. Xin and S. A. Reid, *Chem. Mater.*, 2001, **13**, 3969–3974.

10 A. Ellens, A. Meijerink and G. Blasse, *J. Lumin.*, 1994, **59**, 293–301.

11 G. X. Zhu, M. B. Xie, Q. Yang and Y. L. Liu, *Opt. Laser Technol.*, 2016, **81**, 162–167.

12 S. Y. Z. Chen, L. J. Li, J. Y. Chen, S. J. Xu, W. J. Huang, Z. X. Wen, T. M. Jiang and H. Guo, *J. Mater. Chem. C*, 2023, **11**, 2389–2396.

13 R. G. Kunghatkar, S. J. Dhoble and P. S. Hemne, *Luminescence*, 2016, **31**, 1503–1512.

14 H. Hönigsmann, *Photochem. Photobiol. Sci.*, 2013, **12**, 16–21.

15 M. Deng, Y. Liang, Y. Shi, J. Wang, J. Chen and Q. Liu, *Mater. Sci. Eng., R*, 2024, **159**, 100803.

16 X. Du, H. Zhang, S. F. Zhou, F. T. Zhang, G. P. Dong and J. R. Qiu, *J. Non-Cryst. Solids*, 2015, **420**, 17–20.

17 K. Shionozaki, T. Honma and T. Komatsu, *J. Appl. Phys.*, 2012, **112**, 7.

18 Y. N. Zhuravlev and V. V. Atuchin, *Symmetry*, 2023, **15**, 12.

19 H. Park and J. Barbier, *J. Solid State Chem.*, 2000, **155**, 354–358.

20 Z. G. Hu, M. Yoshimura, K. Muramatsu, Y. Mori and T. Sasaki, *Jpn. J. Appl. Phys., Part 2*, 2002, **41**, L1131–L1133.

21 Y. K. Le, X. J. Huang, H. Zhang, Z. H. Zhou, D. D. Yang, B. Z. Yin, X. F. Liu, Z. G. Xia, J. R. Qiu, Z. M. Yang and G. P. Dong, *Adv. Photonics*, 2023, **5**, 10.

22 M. J. Zhao, Y. T. Tao, P. T. Wang, W. C. Li, D. P. Chen and W. Chen, *Ceram. Int.*, 2024, **50**, 1857–1866.

23 W. Zhang, R. N. Hua, T. Q. Liu, J. Zhao, L. Y. Na and B. J. Chen, *Mater. Res. Bull.*, 2014, **60**, 247–251.

24 V. Singh, G. Sivaramaiah, J. L. Rao, R. S. Kumaran, P. K. Singh, T. S. Kim and L. K. Kim, *J. Mater. Sci.: Mater. Electron.*, 2015, **26**, 5195–5201.

25 H. Segawa, N. A. Wójcik, K. Takahashi, T. Takeda and S. Ali, *J. Am. Ceram. Soc.*, 2024, **107**, 2930–2939.

26 L. C. Ju, X. Xu, L. Y. Hao, Y. Lin and M. H. Lee, *J. Mater. Chem. C*, 2015, **3**, 1567–1575.

27 V. Singh, R. P. S. Chakradhar, J. L. Rao, I. Ko and H. Y. Kwak, *J. Lumin.*, 2010, **130**, 703–708.

28 H. Ebendorff-Heidepriem and D. Ehrt, *J. Phys.: Condens. Matter*, 1999, **11**, 7627–7634.

29 V. Singh, R. P. S. Chakradhar, J. L. Rao and H. Y. Kwak, *J. Lumin.*, 2011, **131**, 247–252.

30 C. M. Brodbeck and L. E. Iton, *J. Chem. Phys.*, 1985, **83**, 4285–4299.

31 D. Y. Lu, L. Zhang and X. Y. Sun, *Ceram. Int.*, 2013, **39**, 6369–6377.

32 D. Y. Lu, S. Z. Cui, Q. L. Liu and X. Y. Sun, *Ceram. Int.*, 2016, **42**, 14364–14373.

33 E. V. Mal'chukova, N. G. Tyurnina, Z. G. Tyurnina and E. I. Terukov, *Glass Phys. Chem.*, 2022, **48**, 363–371.

34 M. Mahfoudhi and N. Oilier, *Opt. Mater.*, 2019, **95**, 7.

35 N. Kunkel and T. Wylezich, *Z. Anorg. Allg. Chem.*, 2019, **645**, 137–145.